Ultrawideband Radar Imaging Using Adaptive Array and Doppler Separation

MOTOSHI ANABUKI, Student Member, IEEE
SHIGEAKI OKUMURA, Student Member, IEEE
TORU SATO, Member, IEEE
Kyoto University, Kyoto, Japan

TAKUYA SAKAMOTO, Member, IEEE
Kyoto University, Kyoto, Japan and University of Hyogo, Himeji, Japan

KENSHI SAHO, Member, IEEE
Ritsumeikan University, Kusatsu, Japan

MOTOTAKA YOSHIOKA
KENICHI INOUE
TAKESHI FUKUDA
HIROYUKI SAKAI, Member, IEEE
Panasonic Corporation, Kyoto, Japan

Manuscript received January 5, 2016; revised June 28, 2016; released for publication August 20, 2016. Date of publication January 9, 2017; date of current version April 17, 2017.

DOI. No. 10.1109/TAES.2017.2649798

Refereeing of this contribution was handled by R. M. Narayanan.

This work was supported in part by the Supporting Program for Interaction-based Initiative Team Studies (SPIRITS) as part of the Japan–Netherlands joint development of sleep monitoring technology using ultrawideband radar, by the Center of Innovation Program (COI), by the Last 5X Innovation R&D Center for a Smart, Happy, and Resilient Society, by the Japan Society for the Promotion of Science KAKENHI Grant 25249057 and Grant 15K18077, and by the R&D project for the expansion of radio spectrum resources or more efficient use of frequency resources for the future, which is supported by the Ministry of Internal Affairs and Communications, Japan.

Authors' addresses: M. Anabuki, S. Okumura, and T. Sato are with the Graduate School of Informatics, Kyoto University, Kyoto 606-8501, Japan, E-mail: (manabuki@sato-lab.0t0.jp; sokumura@sato-lab.0t0.jp; sato.toru.6e@kyoto-u.ac.jp); T. Sakamoto is with the Graduate School of InformaticsKyoto University, Kyoto 606-8501, Japan and also with the Graduate School of Engineering, University of Hyogo, Himeji 671-2280, Japan, E-mail: (t-sakamo@i.kyoto-u.ac.jp); K. Saho is with the College of Science and Engineering, Ritsumeikan University, Kusatsu 525-8577, Japan, E-mail: (saho@fc.ritsumei.ac.jp); M. Yoshioka is with the Interactive AI Research Group, Advanced Research Division, Panasonic Corporation, Kyoto 619-0237, Japan, E-mail: (yoshioka.mototaka@jp.panasonic.com); K. Inoue, T. Fukuda, and H. Sakai are with the Sensing Technology Research Group, Advanced Research Division, Panasonic Corporation, Kyoto 619-0237, Japan, E-mail: (inoue.kenichi@jp.panasonic.com; fukuda.takeshi@jp.panasonic.com; sakai.hiroyuki@jp.panasonic.com).

Ultrawideband Doppler radar interferometry is known as an effective method that enables high-resolution imaging when using a simple antenna array. The technique, however, suffers from image artifacts when multiple moving targets with the similar Doppler velocities are present in the same range bin. To resolve this problem, we combine the Doppler interferometry technique with the Capon methods. Through numerical simulations and experiments, we show the remarkable performance improvement achieved by the proposed method.

I. INTRODUCTION

Ultrawideband (UWB) radar imaging techniques are attracting considerable research attention because of their potential use in security applications, e.g., traffic monitoring for intelligent transport systems, and surveillance systems that can prevent crimes and attacks. While optical cameras are commonly used [1], [2] in security applications, they are unable to monitor targets when their fields of vision are limited by heavy rain, dense fog, or haze. In contrast, UWB radar imaging techniques can continue to monitor targets even when the view is poor.

However, it is difficult to apply conventional UWB radar imaging methods in simple systems, because they involve enormous computational complexity [3]–[6] and require the use of large-scale array antennas [7]–[9].

Recently, radar imaging techniques have been proposed that use only small numbers of antennas [10]–[12]. These techniques are based on the Doppler radar interferometry technique. Applying these techniques to UWB radar, we can provide adequate single pedestrian imaging [13]–[15]. However, the technique suffers from image artifacts that cause the imaging accuracy to deteriorate when multiple targets with similar Doppler velocities are present in the same range bin, because conventional techniques depict the target based on the difference in their Doppler velocity.

To resolve this problem, we use adaptive array-processing methods, which can separate multiple signals using multiantenna arrays [16]. Among the various adaptive array-processing methods [17]–[23] that are available, the Capon method [24], [25] is considered to be classical, but it is still widely used because of its robust performance and simple formulation. The Capon method is a commonly used strategy for the adaptive beamforming technique, which minimizes the output power under a constraint condition that maintains the echo from the angle of interest [24], [25]. However, the performance of this method is limited by the number of antennas available. When the number of targets is greater than the number of available elements, the method does not work. We have, therefore, combined these two techniques. First, we separate the targets based on the Doppler velocity difference. After this process, we apply the Capon method to separate targets that have similar Doppler velocities.

The space-time adaptive processing (STAP) method is a technique that is used to separate a desired signal from interference in the space-time domain. The STAP method is used to increase the probability of target detection in the remote-sensing field [27], [28]. However, this algorithm has

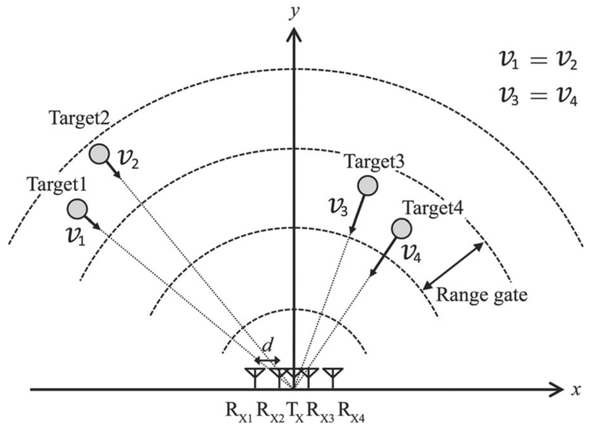

Fig. 1. Schematic of the system model.

enormous computational complexity and requires a large number of antennas. Because imaging systems for security applications typically require real-time imaging and low-cost systems, we use a small number of antennas and reduce the complexity of the process by limiting the number of places where we apply adaptive processing methods. In addition, the STAP method requires reference signals, and when the wrong reference signal is used, the performance of the method deteriorates severely. In contrast, the proposed method does not require reference signals.

This paper presents a high-resolution imaging algorithm for the UWB Doppler radar method and evaluates this algorithm using both simulations and experiments. First, we explain the Doppler radar interferometric imaging algorithm, the range interpolation method, the Capon method, and the false image detection and rejection method. We then examine the simulation results and experimental results obtained using the UWB Doppler radar interferometry technique and show that multiple false images are estimated because of interference of the echo signals that emanate from the targets. To solve this problem while simultaneously minimizing the number of antenna array elements required, we propose a technique that includes both the Doppler radar interferometry technique and the Capon method.

II. SYSTEM MODEL

For simplicity, we consider the method in the form of a 2-D problem. The transmitted signal $s_{\mathrm{T}}(t)$ is a UWB signal that has a center frequency $f_0 = 60.5$ GHz. The wavelength at the center frequency λ is 4.96 mm. The bandwidth is $W = 1.25$ GHz, which corresponds to a downrange resolution of $\Delta r = c/2W = 12.0$ cm, where c is the speed of light. Fig. 1 shows the system model. A transmitting antenna, $\mathrm{T_X}$, and four receiving antennas, $\mathrm{R_{X1}}$, $\mathrm{R_{X2}}$, $\mathrm{R_{X3}}$, and $\mathrm{R_{X4}}$, are set up on the $y = 0$ line, and the receiving antennas form an equal-interval linear antenna array. The positions of the five antennas, $\mathrm{T_X}$, $\mathrm{R_{X1}}$, $\mathrm{R_{X2}}$, $\mathrm{R_{X3}}$, and $\mathrm{R_{X4}}$, are expressed as $(x, y) = (0, 0)$, $(-3d/2, 0)$, $(-d/2, 0)$, $(d/2, 0)$, and $(3d/2, 0)$, respectively, where d is the distance between the receiving antennas. The number of antenna array elements is four, which means that the number of degrees of freedom of the antenna array is three, and the antenna array can, thus, separate a maximum of three signals by the Capon method. The pulse repetition interval is $\Delta T = 0.457$ ms. We then acquire the received signal $s_{il}(t)$ in range bin l using each $\mathrm{R}_{\mathrm{X}i}$.

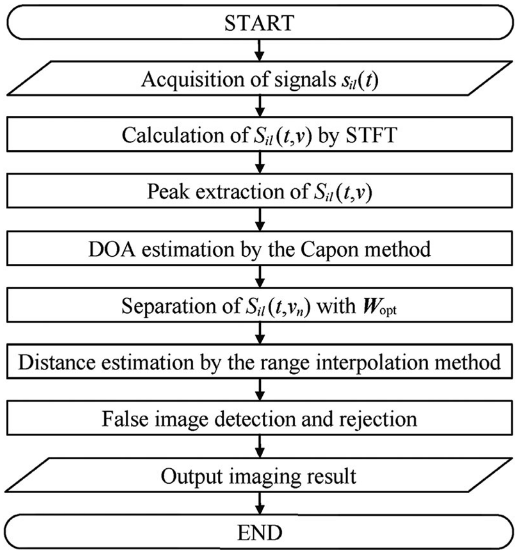

Fig. 2. Procedure for the proposed imaging algorithm.

III. UWB DOPPLER RADAR INTERFEROMETRIC IMAGING ALGORITHM WITH THE CAPON METHOD

A. Doppler Radar Interferometry

The procedure used for the proposed imaging algorithm is summarized in Fig. 2. The algorithm generates images using a combination of the Doppler radar interferometric imaging algorithm, the false image rejection method, and the Capon method.

First, we explain the Doppler radar interferometric imaging algorithm, which can separate multiple echo signals from targets in the frequency domain [10]–[12]. The algorithm estimates the scattering center position for each target using a combination of interferometry and a range interpolation method. If the different moving targets have different radial velocities, they can then be separated using their Doppler frequencies. In this study, the time–frequency distribution $S_{il}(t, v)$ is obtained using a short-time Fourier transform (STFT) of $s_{il}(t)$. $S_{il}(t, v)$ is calculated using

$$S_{il}(t, v) = \int s_{il}(\tau) g(\tau - t) \mathrm{e}^{-j2kv\tau} d\tau \tag{1}$$

where $g(t)$ is the Hamming window function, and k is the wave number of the center frequency. The significant peaks of $S_{il}(t, v)$ are then found for each l using the following conditions:

$$\frac{d|S_{il}(t, v)|}{dv} = 0 \tag{2}$$

$$|S_{il}(t, v)|^2 > \rho \max_{t,v} |S_{il}(t, v)|^2 \tag{3}$$

where ρ is the ratio of the peak extraction threshold power to the maximum power.

Next, we estimate the scattering centers for each of the separate targets on a plane in terms of their distances and their directions of arrival (DOAs). The DOAs of the targets are estimated based on their phase differences using interferometry. The DOAs are calculated using two adjacent elements i and $i+1$ as

$$\psi(t, v_n) = \sin^{-1} \frac{\lambda[\angle S_{il}(t, v_n) - \angle S_{(i+1)l}(t, v_n)]}{2\pi d} \tag{4}$$

where $\angle A$ is the phase of A, and n is the target number.

Based on (4), the DOA estimation accuracy increases when we set a longer value for distance d. However, when we set $d > \lambda/2$, grating lobes appear, and these lobes lead to DOA ambiguity. This problem becomes increasingly serious as the number of targets increases. We have, therefore, determined the distance $d = 0.92\lambda$ empirically, while taking the accuracy of DOA estimation and the effects of the grating lobes into account.

B. High-Accuracy Distance Estimation

The distances $r(t, v_n)$ are estimated by finding the range at which the echo signal intensity is maximized as follows:

$$r_0(t, v_n) = \Delta r \arg\max_{l} |S_{il}(t, v_n)| \tag{5}$$

where Δr is the range resolution. To realize high-resolution imaging, however, it is necessary to estimate the distance to each target more accurately, as opposed to simply using the distance sampling interval. The range interpolation method has, thus, been proposed for this purpose [13]–[15]. The method uses a process of interpolation between the range gates that is based on the echo signal power ratio around the peak. The range interpolation method uses the fractional distance $D(\rho_{\mathrm{P}})$, which was determined via a calibration experiment, to estimate the true distance $r(t, v_n)$.

We explain the calibration experiment. In this experiment, we measured the echo signal power ratio at two adjacent range gates around the peak when the fractional range D $(0 \leq D < \Delta r)$ of a point target was varied. We define P_1 as the maximum power and define P_2 as the higher value of the power at a range gate adjacent to the range gate with the maximum power. The echo signal power ratio is then defined as

$$\rho_{\mathrm{P}}(D) = \frac{P_1}{P_2}. \tag{6}$$

The range interpolation method uses $D(\rho_{\mathrm{P}})$, which is the inverse function of $\rho_{\mathrm{P}}(D)$, to provide an accurate an estimate of the distance to the target. The accurate distance to the targets $r(t, v_n)$ is estimated using

$$r(t, v_n) = r_0(t, v_n) + D(\rho_{\mathrm{P}}). \tag{7}$$

Using the acquired $\psi(t, v_n)$ and $r(t, v_n)$, the target positions $\boldsymbol{x}(t, v_n)$ can then be estimated using

$$\boldsymbol{x}(t, v_n) = \begin{bmatrix} r(t, v_n) \sin\psi(t, v_n) \\ r(t, v_n) \cos\psi(t, v_n) \end{bmatrix}. \tag{8}$$

The UWB Doppler radar interferometric imaging algorithm only uses a small number of antenna array elements for its imaging process. However, this algorithm can only separate targets in terms of their Doppler velocities and their range bins. Consequently, it cannot separate multiple targets with similar Doppler velocities that are present in the same range bin and thus generates false images of these targets.

C. Target Position Estimation Using the Capon Method

To separate targets with similar Doppler velocities, we apply the Capon method to the signal after the separation process in the frequency domain [24]–[26]. The Capon method then estimates the DOAs by minimizing the output power under a constraint condition that maintains the echo from the angle of interest.

Although many high-resolution DOA estimation algorithms are available in addition to the Capon method, including both MUSIC and ESPRIT [29]–[32], it is difficult to determine the signal power accurately using these algorithms. Because we require an accurate echo signal power value to estimate the target distances via the range interpolation method, we use the Capon method because it is advantageous for accurate signal power estimation.

The output power using the Capon method is calculated as follows:

$$\min_{\boldsymbol{W}} P_{\mathrm{out}} = \frac{1}{2}\boldsymbol{W}^{\mathrm{H}} R(t, v_n) \boldsymbol{W}$$

$$\text{subject to } \boldsymbol{a}(\theta)^{\mathrm{T}} \boldsymbol{W}^* = 1 \tag{9}$$

$$R(t, v_n) = \beta R(t - \Delta T, v_n) + (1-\beta) R_0(t, v_n) \tag{10}$$

$$R_0(t, v_n) = \boldsymbol{X}_l^{\mathrm{H}}(t, v_n) \boldsymbol{X}_l(t, v_n) \tag{11}$$

$$\boldsymbol{X}_l(t, v_n) = [S_{1l}(t, v_n)\ S_{2l}(t, v_n) \cdots S_{Nl}(t, v_n)]^{\mathrm{T}} \tag{12}$$

$$\boldsymbol{W} = [w_1\ w_2 \cdots w_N]^{\mathrm{T}} \tag{13}$$

$$\boldsymbol{a}(\theta) = [1\ e^{-jkd\sin\theta}\ e^{-jk2d\sin\theta} \cdots e^{-jkNd\sin\theta}]^{\mathrm{T}} \tag{14}$$

where $\boldsymbol{W}$ is a weight vector, N is the number of antenna array elements in the radar system, $\boldsymbol{a}(\theta)$ is a steering vector, β is a forgetting factor, j is the imaginary unit, $[\cdot]^{\mathrm{H}}$ denotes the Hermitian transpose, $[\cdot]^{\mathrm{T}}$ denotes the transposition, and $[\cdot]^*$ denotes the complex conjugate. We set the initial value $R(0, v_n)$ as follows:

$$R(0, v_n) = \boldsymbol{X}_l^{\mathrm{H}}(0, v_n) \boldsymbol{X}_l(0, v_n). \tag{15}$$

The problem can then be solved by application of Lagrange multiplier methods. The output power of a signal from the direction θ is given by

$$P_{\mathrm{out}}(t, v_n, \theta) = \frac{1}{2\boldsymbol{a}^{\mathrm{H}}(\theta)(R(t, v_n) + \eta I)^{-1} \boldsymbol{a}(\theta)} \tag{16}$$

where η is a diagonal loading factor [33], I is a unit matrix, and A^{-1} denotes the inverse matrix of A. We then estimate the DOAs of each of the targets $\theta_n(t, v_n)$ by searching for the direction θ, at which $P_{\mathrm{out}}(t, v_n, \theta)$ is a maximum for each value of t and v_n.

Next, we estimate the distances to each of the targets. To improve the distance estimation accuracy, we separate the signals using the optimum weight vector. The optimum weight vector of the direction $\theta_n(t, v_n)$ is calculated as follows:

$$\boldsymbol{W}_{\mathrm{opt}}(t, v_n, \theta_n) = \frac{(R(t, v_n) + \eta I)^{-1}\boldsymbol{a}(\theta_n)}{\boldsymbol{a}^{\mathrm{H}}(\theta_n)(R(t, v_n) + \eta I)^{-1}\boldsymbol{a}(\theta_n)}. \quad (17)$$

The separated signal is then calculated using

$$U_l(t, v_n, \theta_n) = \boldsymbol{X}_l^{\mathrm{T}}(t, v_n)\boldsymbol{W}_{\mathrm{opt}}^{*}(t, v_n, \theta_n). \quad (18)$$

We estimate the distances to the targets $p(t, v_n, \theta_n)$ using the range interpolation method exactly like (7), as follows:

$$p(t, v_n, \theta_n) = p_0(t, v_n, \theta_n) + D(\rho_{\mathrm{P}}) \quad (19)$$

$$p_0(t, v_n, \theta_n) = \Delta r \arg\max_{l} |U_l(t, v_n, \theta_n)|. \quad (20)$$

Finally, the target positions $\boldsymbol{y}(t, v_n, \theta_n)$ are given by

$$\boldsymbol{y}(t, v_n, \theta_n) = \begin{bmatrix} p(t, v_n, \theta_n)\sin\theta_n(t, v_n) \\ p(t, v_n, \theta_n)\cos\theta_n(t, v_n) \end{bmatrix}. \quad (21)$$

The proposed method has reduced computational complexity when compared with conventional STAP methods. One typical STAP method applies the Capon method to the signal data in the time-DOA domain [27]. This method, therefore, requires $NQ \times NQ$ matrix inversion, where Q is the number of pulses. When we calculate the inverse matrix via LU decomposition [34], the number of calculation floating point operations (flops) $C_{\mathrm{inv}}(NQ)$ that the calculation process requires is given by

$$C_{\mathrm{inv}}(NQ) = \frac{4}{3}(NQ)^3 - \frac{1}{3}NQ. \quad (22)$$

In contrast, the proposed method applies the Capon method to the signal data only in the DOA domain after the STFT. The proposed method requires fast Fourier transform (FFT) operations [35] to be performed N times and $N \times N$ matrix inversions to be performed Q times, these operations have complexities of $C_{\mathrm{fft}}(Q)$ and $C_{\mathrm{inv}}(N)$, respectively. The number of floating point operations in the FFT for a data length of Q is expressed as

$$C_{\mathrm{fft}}(Q) = 3Q\log_2(Q). \quad (23)$$

In this paper, we use four receiving antennas and a time window of 256 pulses. In this case, the computational complexity of the STAP method is 1.4×10^9 flops, while that of the proposed method is 4.6×10^4 flops. Therefore, the proposed method can reduce the computational complexity considerably when compared with the STAP method.

D. False Image Detection and Rejection Method

To reduce the number of false images produced and improve the overall imaging accuracy, we use a false image detection and rejection method that uses discontinuity in velocity and position [13]–[15]. We apply this method to the image that was acquired using the proposed method. False images often have unrealistically high velocities, and we, therefore, reject any estimated points with high velocities and remove any points that satisfy the following condition:

$$v_{\max} < |\boldsymbol{v}_0(t, v_n, \theta_n)| \quad (24)$$

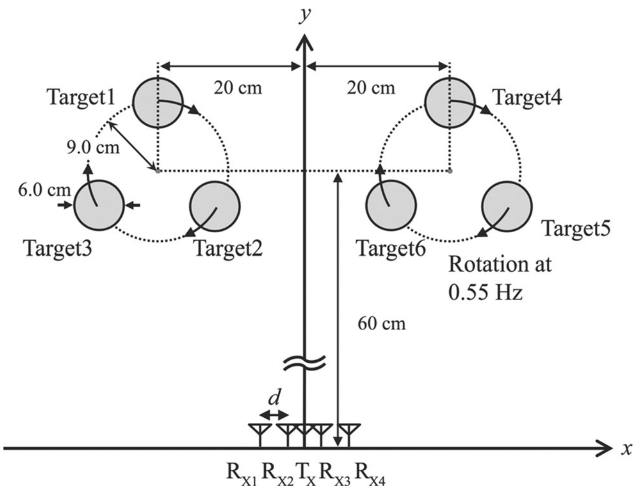

Fig. 3. Schematic of the simulation and experimental model used to evaluate the imaging accuracy.

where $v_{\max}$ is the assumed maximum speed, and $\boldsymbol{v}_0(t, v_n, \theta_n)$ is the velocity that has been calculated using

$$\boldsymbol{v}_0(t, v_n, \theta_n) = \frac{d\boldsymbol{y}(t, v_n, \theta_n)}{dt}. \quad (25)$$

Next, we remove any isolated points, because false images are often found to be isolated. We consider a sphere with radius R_{F} that is centered at $\boldsymbol{y}(t, v_n, \theta_n)$ and then count the number of scattering centers N_{F} present within that sphere. We reject any scattering centers that satisfy the following condition:

$$\frac{N_{\mathrm{F}}}{N_{\mathrm{A}}} < \alpha \quad (26)$$

where N_{A} is the total number of estimated points, and α is the threshold ratio of the number of false points to the total number of estimated points.

IV. RESULTS OF EVALUATION BY SIMULATION

In this section, we examine the performance of the proposed algorithm using numerical simulations. We use the proposed method to estimate the central scattering trajectory of a moving target and thus evaluate the imaging accuracy of the method. In this paper, we use the root-mean-square error (RMSE) between the actual scattering positions and the estimated scattering positions as an evaluation index for imaging accuracy. The RMSE E is calculated using

$$E = \sqrt{\frac{1}{M}\sum\nolimits_{i=1}^{M} \min_{j}\,[(X_{ij} - x_i)^2 + (Y_{ij} - y_i)^2]} \quad (27)$$

where (x_i, y_i) denotes the estimated scattered positions at time $t = i\Delta T$, (X_{ij}, Y_{ij}) denotes the actual scattered positions of target j at time $t = i\Delta T$, and $M\Delta T$ is the total measurement time.

The simulation is performed based on the model shown in Fig. 3. In the simulation, the pulse signal from the radar system is assumed to be a Gaussian-shaped pulse with

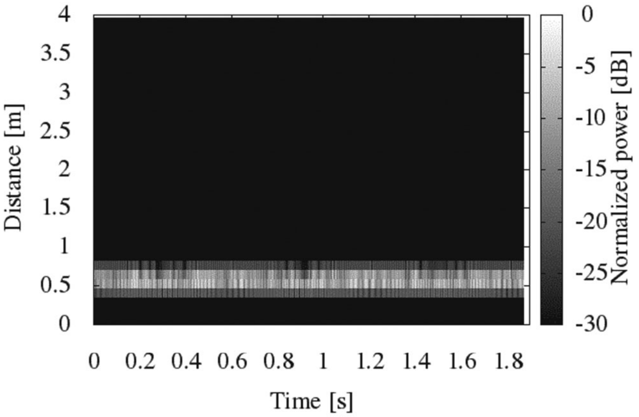

Fig. 4. Power values of echo signals from moving cylindrical targets shown in Fig. 3 in the simulations. The echo signals are in the 0.6–0.72-m range.

10-dB bandwidth of 1.25 GHz. The received signal is then calculated using ray-tracing methods. We consider the effects of both the free-space propagation losses and shadowing.

In the system model shown in Fig. 3, the maximum propagation path difference for both the near-field and far-field models is at most 0.14 mm $= 0.028\lambda$. Therefore, because the difference is sufficiently small compared with the wavelength, it is thus appropriate to apply the far-field propagation model in our study.

We assume a situation in which multiple targets with similar Doppler velocities are present in the same range bin, and we also assume that the number of targets is larger than the number of degrees of freedom of the antenna array. Three cylindrical targets are placed on each of two turntables that are both rotating at the same speed of 0.55 Hz. Each of the target is 6.0 cm in diameter, and the turning radius is 9.0 cm.

Fig. 4 shows the received signal power values. We use the data that were obtained by measuring the targets for 1.9 s. In this figure, we see the echo signals at an approximate distance range of 0.6–0.72 m. Because the targets are located in the same range bin, the echo signals have thus interfered with each other and cannot be separated based on the range difference alone.

Fig. 5 shows the spectrogram that was obtained using the STFT from the echo signals with a window size of $256\Delta T = 117$ ms. The Doppler frequency resolution depends on the window size. A larger window size allows us to separate echoes more accurately in the frequency domain. However, the use of a wide window leads to increased time delays in the system, which is a serious issue in real-time applications. We take these factors into account and subsequently select a window size of $256\Delta T = 117$ ms. The Doppler velocities of each of the six cylindrical targets can be extracted, and each velocity is found to vary periodically. Therefore, there are cases where the Doppler velocities of multiple targets are overlapping.

We have confirmed that the multiple scattering echoes are weak in the actual measurements, and they do not, therefore, significantly affect the experimental results. The multiple scattering echo intensity becomes exponentially smaller each time the scatterings occur. As a result, we did not consider multiple scatterings as part of the simulations.

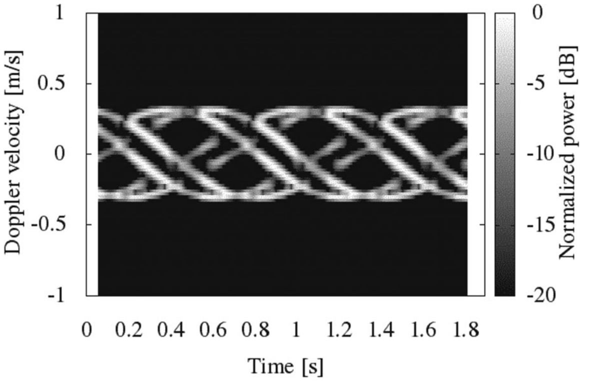

Fig. 5. Spectrogram acquired using STFT from the echo signals shown in Fig. 4 in the simulations. The Doppler velocities of the six targets can then be extracted.

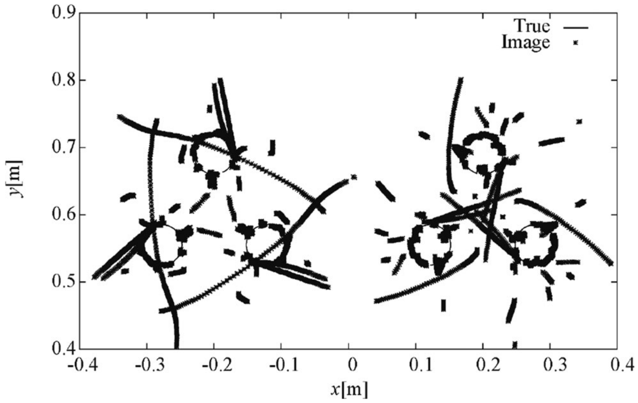

Fig. 6. Image estimated using the UWB Doppler radar interferometric imaging algorithm alone in the simulation. (RMSE: 26 mm.)

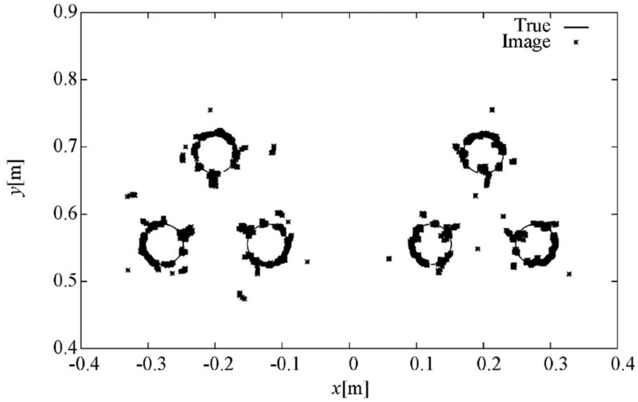

Fig. 7. Image estimated using the UWB Doppler radar interferometric imaging algorithm combined with the false image rejection method in the simulation. (RMSE: 9.5 mm.)

Figs. 6–8 show the imaging results. We used a shape estimation algorithm that compensates for the target motion on the acquired orbits of the scattering centers. In these figures, “true” denotes the actual target contours, and “image” denotes the estimated contours.

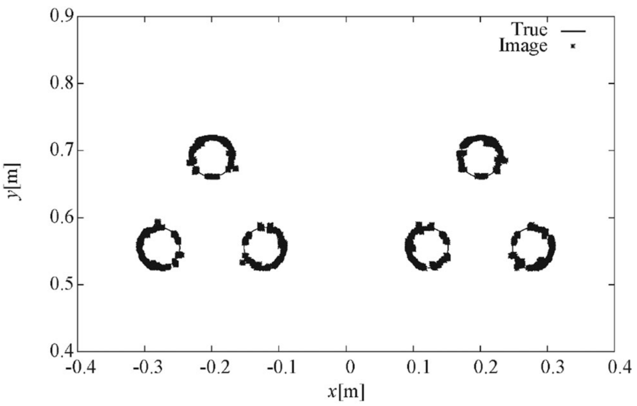

Fig. 8. Image estimated using the proposed algorithm in the simulation. (RMSE: 4.2 mm).

Fig. 6 shows the image that was generated using the UWB Doppler radar interferometric imaging algorithm only. We set $\rho = 0.028$, which is found to produce a false alarm rate of 2.5%. As shown in the figure, multiple false images are present, and the target contours thus cannot be identified. The RMSE is 26 mm, and the total number of estimated points is 16 852. In Fig. 6, the targets on the right and left turntables are imaged differently, while the target setup appears to be symmetrical; this is not actually the case. This is because both of the turntables rotate in a clockwise direction, which actually makes the experimental setup asymmetrical.

Fig. 7 shows the image that was generated in the simulation using the combination of the UWB Doppler radar interferometric imaging algorithm and the false image rejection method. We set $\rho = 0.028$, $v_{\max} = 0.62$ m/s, $R_{\mathrm{F}} = 0.060$ m, and $\alpha = 1/6 \simeq 0.17$. Here, $v_{\max}$ is determined to be 1.5 times the actual maximum target velocity, R_{F} is determined to be the target diameter, and α is selected based on the assumption that the number of estimated scattering points for each target is same. To provide a fair evaluation overall, we selected these parameters to maximize the performance of the conventional method.

Many of the false images have been removed, and the imaging accuracy appears to have improved. However, some false images remain at locations situated away from the contours. The RMSE is 9.5 mm, and the total number of estimated points is 13 228. When compared with the image that was acquired using the UWB Doppler radar interferometric imaging algorithm alone, the RMSE is improved by 63%, and the number of points to be estimated is reduced by 22%.

Fig. 8 shows the image that was generated when using the proposed method in the simulation. Parameters ρ, $v_{\max}$, R_{F}, and α are the same as in the case with Fig. 7, and we set $\beta = 0.925$, empirically. The RMSE is 4.2 mm, and the total number of estimated points is 16 674. The imaging accuracy is improved when compared with that shown in both Figs. 6 and 7. When compared with the image that was obtained using the UWB Doppler radar interferometric imaging algorithm alone, we find that the RMSE is improved by 84%, although the number of points is only reduced by 1.1%. The proposed method, thus, successfully produces high-resolution image while maintaining the same level of data usage.

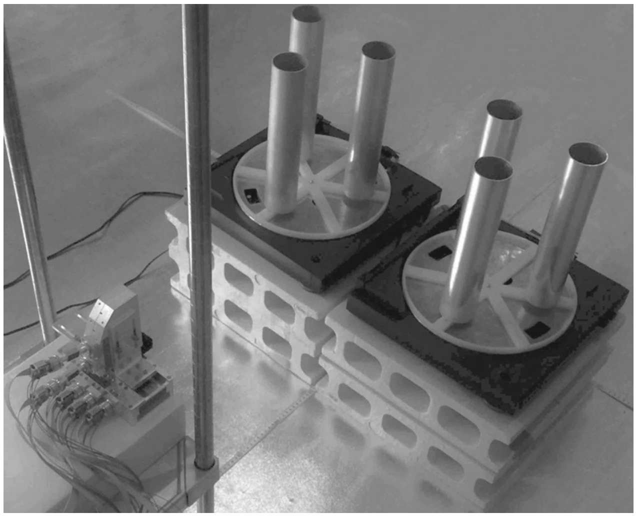

Fig. 9. Photograph of the six targets and the radar system used in the measurements. The targets are 6.0 cm in diameter and 30 cm high. The targets are located on two turntables that rotate at 0.55 Hz.

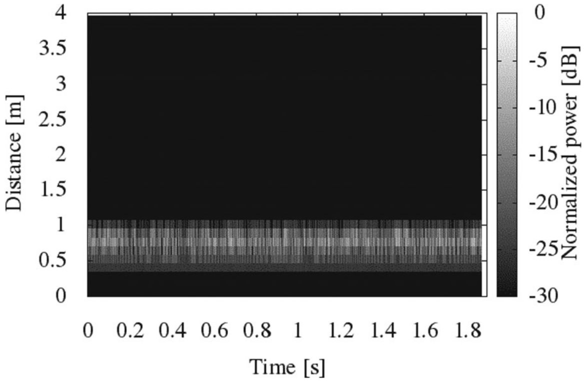

Fig. 10. Power of the echo signals from the moving cylindrical targets in the experiments. The echo signals are in the 0.6- to 0.72-m range.

V. RESULTS OF THE EXPERIMENTAL EVALUATION

In this section, we give the results of the experimental evaluation of the method. The experimental setup shown in Fig. 9 reproduces the setup of the model shown in Fig. 3. In the experiment, the pulse signal of the radar system is a modulated wave composed of a pseudonoise m-sequence with a bandwidth of 1.25 GHz, and the signal is compressed at the receiving end using the same sequence. The parameters used in the experiments are the same as those were used in the simulations.

Fig. 10 shows the received signal power. We use the data that were obtained by measuring the targets for 1.9 s. The figure shows that the echo signals come from an approximate distance range of 0.6–0.72 m. Because the targets are in the same range bin, the echo signals interfere with each other and, thus, cannot be separated using the range bin difference.

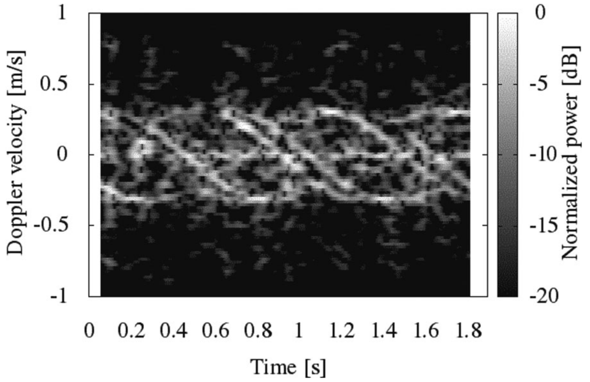

Fig. 11. Spectrogram acquired using the STFT from the echo signals shown in Fig. 10. The Doppler velocities of the six targets were extracted and were found to change periodically.

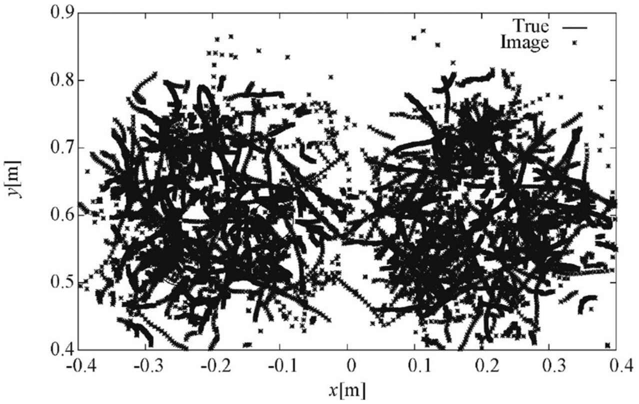

Fig. 12. Image estimated using the UWB Doppler radar interferometric imaging algorithm only and the experimental data. (RMSE: 63 mm.)

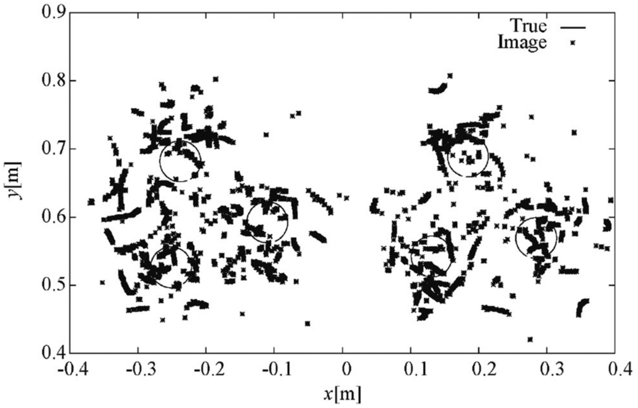

Fig. 13. Image estimated using the UWB Doppler radar interferometric imaging algorithm combined with the false image rejection method and the experimental data. (RMSE: 50 mm.)

Fig. 11 shows the spectrogram that was obtained from the echo signals when using the STFT with a window size of $256\Delta T$ =117 ms. The Doppler velocities of the six cylindrical targets can be extracted, and each of their velocities changes periodically. Therefore, there are cases in which the Doppler velocities of multiple targets are crossed.

Figs. 12–14 show the imaging results that were obtained using the experimental data. We used the same shape estimation algorithm used in the simulation. In these figures, as before, "true" denotes the actual contours of the targets, and "image" denotes the estimated target contours.

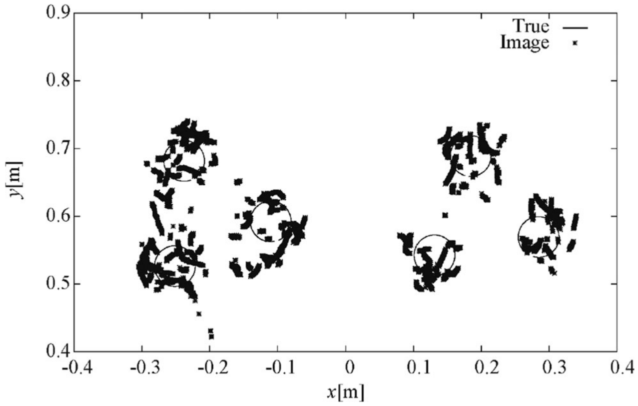

Fig. 14. Image estimated using the proposed algorithm and the experimental data. (RMSE: 26 mm.)

Fig. 12 shows the image that was generated using the UWB Doppler radar interferometric imaging algorithm. We set $\rho = 0.028$. As shown in this figure, multiple false images are present, and therefore, the actual target contours cannot be identified. The RMSE is 63 mm, and the total number of estimated points is 27 653.

In Fig. 13, we show the image that was generated using the combination of the UWB Doppler radar interferometric imaging algorithm and the false image rejection method in the experiments. We set $\rho = 0.028$, $v_{\max} = 0.62$ m/s, $R_{\mathrm{F}} = 0.060$ m, and $\alpha = 0.17$. Most of the false images have been removed in this case, and the imaging accuracy seems to have improved. However, some false images persist at locations away from the actual points of interest. The RMSE is 50 mm, and the total number of estimated points is 8990. When compared with the image that was obtained using the UWB Doppler radar interferometric imaging algorithm alone, the RMSE is improved by 21%, and the number of estimated points is reduced by 67%.

Fig. 14 presents the image that was generated by the proposed method in the experiments. Parameters ρ, $v_{\max}$, R_{F}, and α are the same as in the case with Fig. 13, and we set $\beta = 0.925$. The RMSE is 26 mm in this case, and the total number of estimated points is 11 016. The imaging accuracy is obviously improved when compared with that shown in both Figs. 12 and 13. When compared with the image that was obtained using the UWB Doppler radar interferometric imaging algorithm alone, the RMSE is improved by 59%, while the total number of estimated points is reduced by only 60%. The proposed method, thus, also succeeds in producing high-resolution images while suppressing the reduction of data usage in the experiment.

Differences in the imaging accuracy of the proposed method can be observed between the simulation Fig. 8 and measurement Fig. 14. This difference is considered to have been partly caused by excessive phase noise in the radar system that was used in our study; each of the four receivers uses its own local oscillator, and these do not use the same local reference signal.

VI. CONCLUSION

In this paper, we proposed a new UWB radar imaging algorithm that uses a combination of the UWB Doppler radar interferometric imaging algorithm, a false image detection and rejection method, and the Capon method. First, we explained the operation of each of these three methods. Then, we explained the disadvantages of the conventional approach, which include false image generation, reduced imaging reliability, and the complexity of the required system. Next, we evaluated the imaging accuracy of the proposed method through simulations. In these simulations, we assumed that multiple targets were moving in the same range bin. The proposed method could generate images with a high accuracy of 4.2 mm and could improve the imaging accuracy by 55% when compared with the image that was acquired using the combination of the UWB Doppler radar interferometric imaging algorithm and the false image rejection method. Finally, we evaluated the imaging accuracy of the proposed method experimentally. The proposed method could generate images with a high accuracy of 26 mm and could improve the imaging accuracy by 47% when compared with that of the image generated using the combination of the UWB Doppler radar interferometric imaging algorithm and the false image rejection method. In both the simulations and the experiments, the proposed method produced more accurate images than the conventional methods.

REFERENCES

[1] Y. Hohikawa, Y. Hashimoto, A. Moro, K. Terabayashi, and K. Umeda
Tracking of human groups using subtraction stereo
SICE J. Control Meas. Syst. Integr., vol. 4, no. 3, pp. 214–220, 2011.

[2] K. Schindler, A. Ess, B. Leibe, and L. V. Gool
Automatic detection and tracking of pedestrians from a moving stereo rig
ISPRS J. Photogramm. Remote Sens., vol. 65, no. 6, pp. 523–537, 2010.

[3] X. Zhuge and A. G. Yarovoy
A sparse aperture MIMO-SAR-based UWB imaging system for concealed weapon detection
IEEE Trans. Geosci. Remote Sens., vol. 49, no. 1, pp. 509–518, Jan. 2011.

[4] S. Bertl, A. Dallinger, and J. Detlefsen
Interferometric focusing for the imaging of humans
IET Radar Sonar Navigat., vol. 4, no. 3, pp. 457–463, 2010.

[5] Y. Jin and J. M. F. Moura
Time-reversal detection using antenna arrays
IEEE Trans. Signal Process., vol. 57, no. 4, pp. 1396–1414, Apr. 2009.

[6] Y. Chen, E. Gunawan, K. S. Low, S. Wang, C. B. Soh, and T. C. Putti
Time-reversal ultrawideband breast imaging: Pulse design criteria considering multiple tumors with unknown tissue properties
IEEE Trans. Antennas. Propag., vol. 56, no 9, pp. 3073–3077, Sep. 2008.

[7] T. Sakamoto
A fast algorithm for 3-dimensional imaging with UWB pulse radar systems
IEICE Trans. Commun., vol. E90-B, no. 3, pp. 636–644, 2007.

[8] S. Kidera, T. Sakamoto, and T. Sato
High-resolution and real-time three-dimensional imaging algorithm with envelopes of spheres for UWB radars
IEEE Trans. Geosci. Remote Sens., vol. 46, no. 11, pp. 3503–3513, Nov., 2008.

[9] T. C. Williams, J. M. Sill, and E. C. Fear
Breast surface estimation for radar-based breast imaging system
IEEE Trans. Biomed. Eng., vol. 55, no. 6, pp. 1678–1686, Jun. 2008.

[10] A. Lin and H. Ling
Doppler and direction-of-arrival (DDOA) radar for multiple-mover sensing
IEEE Trans. Aerosp. Electron. Syst., vol. 43, no. 4, pp. 1496–1509, Oct. 2007.

[11] A. Lin and H. Ling
Frontal imaging of human using three-element Doppler and direction-of-arrival radar
Electron. Lett., vol. 42, no. 11, pp. 660–661, May 2006.

[12] A. Lin and H. Ling
Three-dimensional tracking of humans using very low-complexity radar
Electron. Lett., vol. 42, no. 18, pp. 1062–1063, Aug. 2006.

[13] K. Saho, T. Sakamoto, T. Sato, K. Inoue, and T. Fukuda
Pedestrian imaging using UWB Doppler radar interferometry
IEICE Trans. Commun., vol. E96-B, no. 2, pp. 613–623, 2013.

[14] K. Saho, T. Sakamoto, T. Sato, K. Inoue, and T. Fukuda
Accurate and real-time pedestrian classification based on UWB doppler radar images and their radial velocity features
IEICE Trans. Commun., vol. E96-B, no. 10, pp. 2563–2572, 2013.

[15] K. Saho, T. Sakamoto, T. Sato, K. Inoue, and T. Fukuda
Accurate image separation method for two closely spaced pedestrians using UWB doppler imaging radar and supervised learning
IEICE Trans. Commun., vol. E97-B, no. 6, pp. 1223–1233, 2014.

[16] B. Widrow, P. E. Mantey, L. J. Griffiths, and B. B. Goode
Adaptive antenna systems
Proc. IEEE, vol. 55, no. 12, pp. 2143–2159, Dec. 1967.

[17] S. D. Somasundaram
Wideband robust Capon beamforming for passive sonar
IEEE J. Ocean. Eng., vol. 38, no. 2, pp. 308–322, Apr. 2013.

[18] X. Yang, L. Yan, Y. Sun, and T. Zeng
Improved orthogonal projection approach utilizing interference covariance matrix reconstruction for adaptive beamforming
Electron. Lett., vol. 50, no. 20, pp. 1446–1447, Sep. 2014.

[19] M. Costa and V. Koivunen
Application of manifold separation to polarimetric Capon beamformer and source tracking
IEEE Trans. Signal Process., vol. 62, no. 4, pp. 813–827, Feb. 2014.

[20] S. D. Somasundaram, N. H. Parsons, P. Li, and R. C. D. Lamare
Reduced-dimension robust Capon beamforming using Krylov-subspace techniques
IEEE Trans. Aerosp. Electron. Syst., vol. 51, no. 1, pp. 270–289, Jan. 2015.

[21] L. Huang, J. Zhang, X. Xu, and Z. Ye
Robust adaptive beamforming with a novel interference-plus-noise covariance matrix reconstruction method
IEEE Trans. Signal Process., vol. 63, no. 7, pp. 1643–1650, Apr. 2015.

[22] J. Zhuang, Q. Ye, Q. Tan, and A. H. Ali
Low-complexity variable loading for robust adaptive beamforming
Electron. Lett., vol. 52, no. 5, pp. 338–340, Mar. 2016.

[23] Z. Zhang, W. Liu, W. Leng, A. Wang, and H. Shi
Interference-plus-noise covariance matrix reconstruction via spatial power spectrum sampling for robust adaptive beamforming
IEEE Trans. Signal Process., vol. 23, no. 1, pp. 121–125, Jan. 2016.

[24] J. Capon
High-resolution frequency-wavenumber spectrum analysis
Proc. IEEE, vol. 57, no. 8, pp. 1408–1418, Aug. 1969.

[25] R. D. Palmer, S. Gopalam, T.-Y. Yu, and S. Fukao
Coherent radar imaging using Capon's method
Radio Sci., vol. 33, no. 6, pp. 1585–1598, 1998.

[26] B. Liao, S.-C. Chan, and K. -M. Tsui
Recursive steering vector estimation and adaptive beamforming under uncertainties
IEEE Trans. Aerosp. Electron. Syst., vol. 49, no. 1, pp. 489–501, Jan. 2013.

[27] W. L. Melvin
A STAP overview
Proc. IEEE, vol. 19, no. 1, pp. 19–35, Jan. 2004.

[28] J. Ward
Maximum likelihood angle and velocity estimation with space-time adaptive processing radar
in *Proc. Conf. Rec. Asilomar Conf. Signals, Syst., Comput.*, Nov. 1996, pp. 1265–1267.

[29] R. O. Schmidt
Multiple emitter location and signal parameter estimation
IEEE Trans. Antennas. Propag., vol. AP-34, no. 3, pp. 276–280, Mar. 1986.

[30] R. Roy, A. Paulraj, and T. Kailath
ESPRIT—A subspace rotation approach to estimation of parameters of cisoids in noise
IEEE Trans. Acoust., Speech, Signal Process., vol. ASSP-34, no. 5, pp. 1340–1342, Oct. 1986.

[31] R. Roy and T. Kailath
ESPRIT-estimation of signal parameters via rotational invariance techniques
IEEE Trans. Acoust., Speech, Signal Process., vol. 37, no. 7, pp. 984–995, Jul. 1989.

[32] T. B. Lavate, V. K. Kokate, and A. M. Sapkal
Performance analysis of MUSIC and ESPRIT DOA estimation algorithms for adaptive array smart antenna in mobile communication
in *Proc. 2nd Int. Conf. Comput. Netw. Technol.*, Apr. 2010, pp. 308–311.

[33] K. Takao and N. Kikuma
An adaptive array utilizing an adaptive spatial averaging technique for multipath environments
IEEE Trans. Antennas Propag., vol. AP-35, no. 12, pp. 1389–1396, Dec. 1987.

[34] S. C. Chapra and R. P. Canale
Numerical Methods for Engineers. New York, NY, USA: McGraw-Hill.

[35] J. W. Cooley and J. W. Tukey
An algorithm for machine computation of complex Fourier series
Math. Comput., vol. 19, pp. 297–301, 1965.

Motoshi Anabuki (S'15) received the B.E. degree in electrical engineering in 2015 from Kyoto University, Kyoto, Japan, where he is currently working toward the M.I. degree at the Graduate School of Informatics.

His research interests include ultrawideband radar imaging and signal processing.

Shigeaki Okumura (S'13) received the B.E. degree in electrical engineering from Kyoto University, Kyoto, Japan, in 2013, and the M.I. degree in communications and computer engineering in 2015 from the Graduate School of Informatics, Kyoto University, where he is currently working toward the Ph.D. degree.

His current research interests include ultrawideband radar imaging, medical ultrasound imaging, and signal processing.

Mr. Okumura has been a Research Fellow (DC1) of the Japan Society for the Promotion of Science since 2015.

Takuya Sakamoto (M'04) received the B.E. degree in electrical and electronic engineering from Kyoto University, Kyoto, Japan, in 2000, and the M.I. and Ph.D. degrees in communications and computer engineering from the Graduate School of Informatics, Kyoto University, in 2002 and 2005, respectively.

From 2006 to 2015, he was an Assistant Professor at the Graduate School of Informatics, Kyoto University. From 2011 to 2013, he was also a Visiting Researcher at Delft University of Technology, Delft, The Netherlands. Since 2015, he has been an Associate Professor at the Graduate School of Engineering, University of Hyogo, Himeji, Japan. He has also been a part-time Researcher at the Graduate School of Informatics, Kyoto University, since 2015. His current research interests include ultrawideband radar, radar imaging, and radar signal processing.

Dr. Sakamoto received the Best Paper Award from the International Symposium on Antennas and Propagation (ISAP) in 2004, the Young Researcher's Award from the Institute of Electronics, Information and Communication Engineers (IEICE) in 2007, the Best Presentation Award from the Institute of Electrical Engineers of Japan in 2007, the Best Paper Award from the IEICE Communication Society in 2007, the Best Paper Award from ISAP 2012, and the Masao Horiba Award in 2016.

Kenshi Saho (M'14) received the B.E. degree in electrical and electronic engineering, and the M.I. and Ph.D. degrees in communications and computer engineering from Kyoto University, Kyoto, Japan, in 2008, 2010, and 2013, respectively.

Since 2014, he has been an Assistant Professor with the College of Science and Engineering, Ritsumeikan University, Kusatsu, Japan. His research interests include signal-processing techniques for radar/sonar imagers, sensor fusion systems for positioning and tracking, and micro-Doppler sensors.

Dr. Saho is a member of the Institute of Electronics, Information and Communication Engineers of Japan (IEICE), and the Institute of Electrical Engineers of Japan. He received the Researcher's Award from the IEICE Intelligent Transportation Systems technical committee in 2016, the Excellent Oral Presentation Award at the International Conference on Intelligent and Automation Systems in 2015, the Young Researcher's Award from the Radiation Science Society of Japan in 2013, and the Best Paper Award at the International Symposium on Antennas and Propagation in 2012.

Toru Sato (M'92) received the B.E., M.E., and Ph.D. degrees in electrical engineering from Kyoto University, Kyoto, Japan, in 1976, 1978, and 1982, respectively.

Since 1983, he has been with Kyoto University, where he is currently a Professor in the Department of Communications and Computer Engineering, Graduate School of Informatics. His major research interests include system design and signal-processing aspects of ultrawideband radars, atmospheric radars, radar remote sensing of the atmosphere, and biomedical imaging.

Dr. Sato is a Fellow of the Institute of Electronics, Information, and Communication Engineers of Japan and a member of the Society of Geomagnetism and Earth, Planetary and Space Sciences, the Japan Society for Aeronautical and Space Sciences, the Institute of Electrical and Electronics Engineers, and the American Meteorological Society.

Mototaka Yoshioka received the B.S. and M.S. degrees in electrical and electronic engineering from Tokyo Institute of Technology, Tokyo, Japan, in 2001 and 2003, respectively.

In 2003, he joined the Advanced Technology Research Laboratory, Matsushita Electronics Corporation (currently Panasonic Corporation), Kyoto, Japan, where he was involved in the research and development of automotive navigation systems, wearable sensors, and vital sensors. He passed the patent attorney examination in 2008. His research interests include signal processing of vital sign and wearable/noncontact biosensing systems.

Kenichi Inoue received the B.S. and M.S. degrees in electronic science and engineering from Kyoto University, Kyoto, Japan, in 2000 and 2002, respectively.

In 2002, he joined the Semiconductor Device Research Center, Semiconductor Company, Matsushita Electric Industrial Co. Ltd., Osaka, Japan, where he worked on semiconductor laser devices, sensor devices, and systems. Since 2009, he has been with the Advanced Research Division, Panasonic Corporation, Kyoto, where he is involved in the research and development of ultrawideband radar sensor systems and their applications.

Mr. Inoue is a member of the Japan Society of Applied Physics and the Institute of Electronics, Information and Communication Engineers of Japan.

Takeshi Fukuda was born in Osaka, Japan, in 1969. He received the B.S. and M.S. degrees in electronic engineering from Osaka University, Suita, Japan, in 1993 and 1995, respectively.

In 1995, he joined the Electronics Research Laboratory, Matsushita Electronics Corporation, Osaka, where he was involved in the research and development of microwave-integrated circuits. Since 2015, he has been with the Advanced Research Division, Panasonic Corporation, Kyoto, Japan. His current research interests include algorithms and radio-frequency architectures for high-resolution millimeter-wave radar systems.

Hiroyuki Sakai (M’86) was born in Osaka, Japan. He received the B.S. and M.S. degrees in electrical engineering from Osaka University, Osaka, in 1984 and 1986, respectively.

In 1986, he joined the Semiconductor Research Center, Matsushita Electric Industrial Co., Ltd., Osaka, and was involved in research and development of high-speed GaAs digital integrated circuits (ICs). From 1991 to 1992, he took an active part in the development of GaAs radio-frequency (RF) ICs for very compact cellular phones. In 1993, he started to research and develop the millimeter-wave devices and its ICs. In 1995, he joined the Electronics Research Laboratory, Matsushita Electronics Corporation, Osaka, and continued his research and development on millimeter-wave devices, particularly a new millimeter-wave IC concept named millimeter-wave flip-chip IC. From 1998 to 2000, he visited Stanford University, Stanford, CA, USA, as a Visiting Scholar, expanded his research subjects to new Si-based RF devices and their integration technologies. He is currently a Chief Researcher of the Advanced Research Division, Panasonic Corporation, Kyoto, Japan.

Mr. Sakai was a Secretary of the IEEE Electron Devices Society Kansai Chapter from 2002 to 2003. He was a member of the Technical Program Committee of the IEEE International Solid-State Circuit Conference from 2002 to 2008.